Preprints (www.preprints.org) | NOT PEER-REVIEWED | Posted: 19 May 2023 doi:10.20944/preprints202305.1428.v1

Disclaimer/Publisher's Note: The statements, opinions, and data contained in all publications are solely those of the individual author(s) and contributor(s) and not of MDPI and/or the editor(s). MDPI and/or the editor(s) disclaim responsibility for any injury to people or property resulting from any ideas, methods, instructions, or products referred to in the content.

Article

Study on cubic-orientation settlement of angiotensin converting enzyme II immobilized on polystyrene by molecular dynamics simulation

Yang Ma [1] and Yong J. Yuan [1,2,*]

[1] Laboratory of Biosensing and MicroMechatronics, Southwest Jiaotong University, Chengdu, Sichuan 610031, P. R. China; yongyuan@swjtu.edu.cn

[2] Bond-Rupture Solutions, 601 St. Kilda Road, Melbourne, Vic 3004, Australia; yongyuan@outlook.com

* Correspondence: yongyuan@outlook.com; yongyuan@swjtu.edu.cn

Abstract: The adsorption of proteins on polymer is widely used in biosensors. Here, molecular dynamics (MD) simulation was used to study the immobilization of angiotensin converting enzyme II (ACE2) with six initial orientations proposed on polystyrene (PS) at the ambient conditions of pH (4.5, 6, 7, 8, 9.5) and NaCl（0.01, 0.05, 0.1, 0.15, 0.2, 0.25 M). ACE2 immobilization under favorable ambient conditions was characterized by minimum distance (*short*), settlement time (*fast*), interaction energy (*substantial*) and protein configuration (*stable*). ACE2 orientations proposed in 0.15M NaCl were respectively preferable to (90, 0, 0), (0, 0, 0) and (0, 270, 0), (180, 0, 0) and (0, 90, 0), (90, 0, 0) at pH 4.5, 6, 7, 9.5. ACE2 immobilization was further evaluated at pH 7 by optimizing NaCl concentration. Its proposed orientations of (i) (0, 270, 0), (ii) (0, 0, 0) and (90, 0, 0), and (iii) (0, 90, 0) and (90, 0, 0) were preferable in 0.05, 0.1 and 0.2 M NaCl, respectively. The great significance of cubic-orientation settlement mode provides tangible improvement for the microfabrication of biochips for rapid diagnosis of severe acute respiratory syndrome coronavirus II (SARS-CoV-2).

Keywords: Angiotensin converting enzyme II; Polystyrene; Molecular dynamics simulation; Adsorption behaviors; Biochips

1. Introduction

Protein adsorption on polymer membranes is reflected in many important applications, such as biomaterials [1,2], marine antifouling [3,4], diagnostic tools [5–7], food processing and packaging [8,9], health equipment [10,11], and medical products [12,13]. Polymer films with or without protein coating showed completely different characteristics, especially immobilization of specific proteins on surface acoustic wave (SAW) delay lines for biosensing applications [14]. Therefore, understanding the adsorption process of protein and polymer is very important for predicting, controlling, and manipulating protein adsorption to design suitable composite membranes for expected applications [15]. The adsorption of protein on the polymer surface is complex. The charge distribution of protein and polymer [16,17], hydrophobicity [18,19], protein size [20,21], structural stability [18,22], polymer molecular weight [23–25], surface morphology [26–28], chemical properties [29–31], as well as ambient temperature [32], pH value [17,33], ionic strength [34,35] have significant effects on the adsorption process.

The adsorption of protein on polymer has been widely reported [36–41] as summarized in Table 1. The protein adsorption mechanism mainly focuses on one or more of van der Waals (VDW), electrostatic and hydrophobic interactions. The interaction of bovine serum albumin (BSA) and poly (carboxybetaine methacrylate) (PCBMA) and hydrophilic poly [oligo(ethylene glycol) methyl ether methacrylate] (POEGMA) in NaCl aqueous solution was studied by total internal reflection microscope (TIRM) [36]. Both surface charge and polymer brush length affect protein adsorption through electrostatic repulsion and spatial repulsion, respectively. The adsorption mechanism of BSA on polyvi-

© 2023 by the author(s). Distributed under a Creative Commons CC BY license.

Preprints (www.preprints.org) | NOT PEER-REVIEWED | Posted: 19 May 2023 doi:10.20944/preprints202305.1428.v1

nylidene difluoride (PVDF) surface was investigated by surface tension components (STC) and Hansen solubility parameters (HSP) theory [37]. The immobilization of BSA on the polymer was determined by static adsorption experiments. There was no direct correlation between the adsorption capacity of BSA and HSP, and the immobilized BSA was increased with increasing VDW component of surface tension. The comprehensive characterization of BSA on polyethersulfone (PES) surface was conducted by scanning electron microscope (SEM), attenuated total reflection-Fourier transform infrared (FTIR), contact angle, zeta potential [38]. Surface charge density measurement showed that the adsorption of BSA on PES was irreversible at pH > 4.7 due to the strong electrostatic interaction between BSA and PES. The amount of β-lactoglobulin adsorbed on PES membrane was calculated by Freundlich adsorption isotherm model [39]. The β-lactoglobulin dimer structure was dissociated into a monomer structure under acidic and alkaline conditions, and the hydrophobic interaction between the protein and the membrane enhanced the protein adsorption. The interaction between different immunoglobulins (IgG, IgA, IgM) and polystyrene (PS) nanoparticles with different surface charges [40], showed that different immunoglobulins had favorable interactions with neutral charged surfaces, and hydrophobic interactions were crucial for the adsorption of proteins and nanoparticles. Single-molecule microscopy was used to study the kinetics of α-Lactalbumin (α-LA) and Lysozyme at the interface of uncharged PS with different molecular weights [41]. The α-LA showed interfacial adsorption-desorption, while lysozyme experienced random walk at the interface, and the residence time of the two proteins depended on the molecular weight of the polymer. If the short-range hydrophobic interaction was dominated, the blocking kinetics displayed by lysozyme is determined by the free volume of PS.

Table 1. Study on protein and polymer adsorption.

Protein	Polymers	Environment	Interaction	Method/ theory
BSA	POEGMA 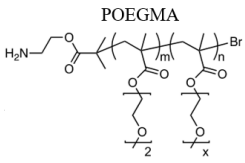 PCBMA 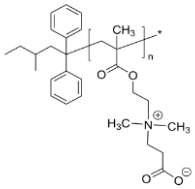	NaCl aqueous solution	Electrostatic [36]	TIRM
	PVDF 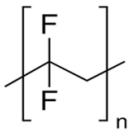	Phosphate buffer solution (PBS pH 7.0, 0.1 M)	VDW [37]	STC, HSP
BSA	PES 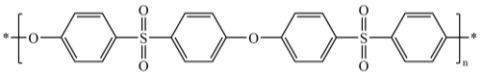	pH 4.7, 7, 10 NaCl solution	Electrostatic [38]	Contact Angle, FTIR
β-lactoglobulin		PBS (pH 3, 5.2, 7, 9.5)	Hydrophobic [39]	Freundlich model
IgG、IgA、IgM	PS 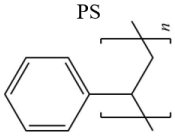	PBS	Electrostatic Hydrophobic [40]	Zeta potential
α-LA、Lysozyme		10 mM HEPES buffer (pH 7.2)	Hydrophobic [41]	TIRM

Mussel protein	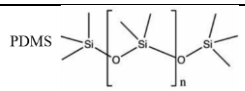 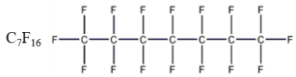		VDW Electrostatic [42]	
FN	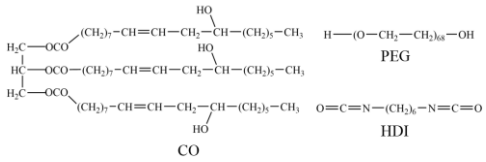		VDW Electrostatic [43]	
	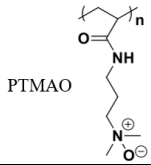	water	Hydrogen bonds [44]	MD
FB、HSA	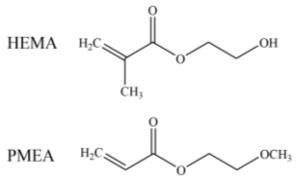		VDW Electrostatic Hydrogen bonds [45]	
HSA、FN	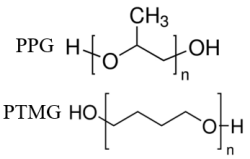		Hydrophobic Hydrogen bonds [46]	

Despite experimental studies given an account of protein immobilization, it is still challenging to understand its molecular mechanism. The implementation of molecular dynamics (MD) is beneficial to understand protein and polymer interaction phenomena [42–46]. The mussel protein on polydimethylsiloxane (PDMS) and C_7F_{16}-SAM surfaces [42] was supposed to be a large conformational change, due to its hydrophobic residues facing outward. The potential of mean force (PMF) indicated that the binding ability of water molecules to PDMS had an important effect on a better combination with the membrane. The interplay between fibronectin (FN) and poly (ethylene glycol) and castor oil copolymers of hexamethylene diisocyanate-based polyurethanes (PEG-HDI and CO-HDI, respectively) [43], concentrates hydrophobic residues at the N-terminal end of FN. The polymer surface determines the overall protein adsorption affinity, due to its roughness. Poly (trimethylamine N-oxide) (PTMAO) zwitterionic polymer was designed to study its adsorption behavior with FN [44]. The strong hydration of PTMAO surface could cause less protein adsorption. The interaction of fibrinogen (FB) and human serum albumin (HSA) with 2-hydroxymethyl methacrylate (HEMA) and poly (2-methoxyethyl acrylate) (PMEA) membranes [45] were investigated. The binding strength between PMEA and FB was relatively weakened while hydrogen bonds dominated. The effect of polyurethane (PU) with different crosslinking densities of polypropylene glycol (PPG) and polytetramethylene glycol (PTMG)—interacting HSA and FN [46]—was determined by PEG concentration due to increasing hydrophobicity. As summarized in Table 1, most of MD research focuses on anti-fouling, the simulation modelling is relatively simple. A feasible study on immobilizing proteins on SAW delay line [47] therefore become inevitable to further application and development of SAW based biosensors [48] for rapid diagnostic tools.

COVID-19 caused by severe acute respiratory syndrome coronavirus II (SARS-CoV-2) has developed into a serious global public health event. If COVID-19 never goes away completely, it will be classified as an endemic disease. The entry of SARS-CoV-2 into target cells through its receptor angiotensin converting enzyme II (ACE2) will trigger various protective reactions, leading to severe lower respiratory tract infection and acute respiratory distress syndrome [49,50]. The immobilization of ACE2 on polymer membranes is beneficial to the development of biochips for the rapid diagnosis

of SARS-CoV-2. Here, the interaction of ACE2 and PS was thoroughly investigated by MD to pave the instructive way of fabricating SARS-CoV-2 biochips for combatting the global COVID-19 pandemic. The adsorption behaviors of ACE2 based on a cubic-orientation-settlement model was proposed with six initial orientations on PS surface at ambient temperature, according to minimum distance between ACE2 and PS. The interaction energy between ACE2 and PS was calculated, indicating the stability of ACE2 immobilized.

2. Modelling and Methods

2.1 PS membrane structure

The chemical formula of PS is supposed to be $(C_8H_8)_n$, where *n* is the number of repeating units. PS monomer units were constructed using chemical modeling programs by the ORCA program [51]. The B3LYP and ωB97M-V functionals were used to optimize the geometric structure and calculate the single point energy [52]. The atomic charge of RESP (Restrained ElectroStatic Potential) [53] was calculated by the Multiwfn program, which evaluates the electrostatic potential involved in the analysis based on the efficient algorithm proposed in Reference [54]. The generalized AMBER force field is used to determine the intramolecular and intermolecular force constants of PS units [55]. The initial PS film was constructed randomly by 180 polymer chains in a 25×25×4 nm container. Each polymer chain has 10 PS monomer units, as shown in Figure 1a.

All simulations were performed using the GROMACS (version 2021.5) program [56]. After initial PS was conducted by the energy minimization optimization configuration as shown in Figure 1b, the velocity rescaling with a coupling time of 0.1 ps was at 300 K for 20 ns NVT simulation in Figure 1c. Finally, a Parrinello-Rahman pressure stabilizer with a coupling time of 2 ps is at 1 atmosphere for 30 ns NPT simulation in Figure 1d. During NPT simulation, the temperature was initially increased to 500 K at a rate of 0.02 K/ps, then decreased to 300 K at the same rate, maintaining at 300 K until the end of the simulation [57]. The PS density (12.4×12.4×2.0 nm) was 1.02 g/cm^3, which was close to the experimental density of 1.05 g/cm^3 [58].

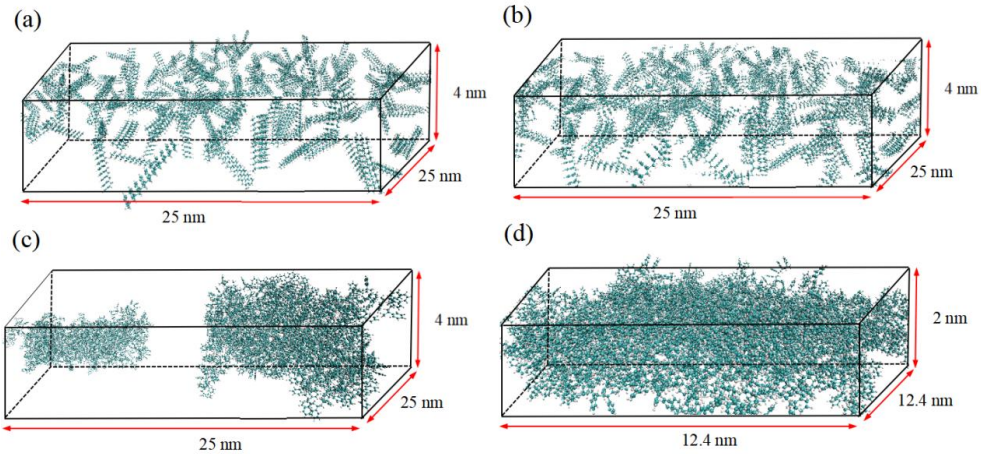

Figure 1. The morphology of PS simulation process. **(a)** initial PS. **(b)** energy minimization, **(c)** NVT pre-equilibrium, **(d)** NPT simulation.

2.2 ACE2 Structure and Charge

The three-dimensional ACE2 structure as shown in Figure 2a was derived from the protein database (PDB ID: 1R42) [59], and the ligand was deleted using the VMD (version 1.9.3) program [60]. The structure contains a total of 597 amino acid residues as illustrated in Table S1 as charged and not charged. Swiss PDB Viewer (version 4.1.0) was used to check the protein structure for missing atoms [61]. The pK_a value and total charge of amino acid residues of ACE2 under different conditions were calculated by H++ program [62]. The AMBER99sb force field was to simulate the parameters of ACE2 [63]. The protonation process of ACE2 was performed by GROMACS. Specifically, the protonation states of acidic and basic amino acids were determined by the pH and pK_a values of the side chain

and terminal –NH_2/–COOH groups [64]. GROMACS allows the manipulation of the protonated state of these five amino acid groups, such as ASP and GLU with carboxylic acid groups on their side chains, while acidic LYS, CYS and HIS with amino, thiol and imidazole rings on their side chains are alkaline. The total charge of ACE2 calculated based on pK_a values is shown in Table S2.

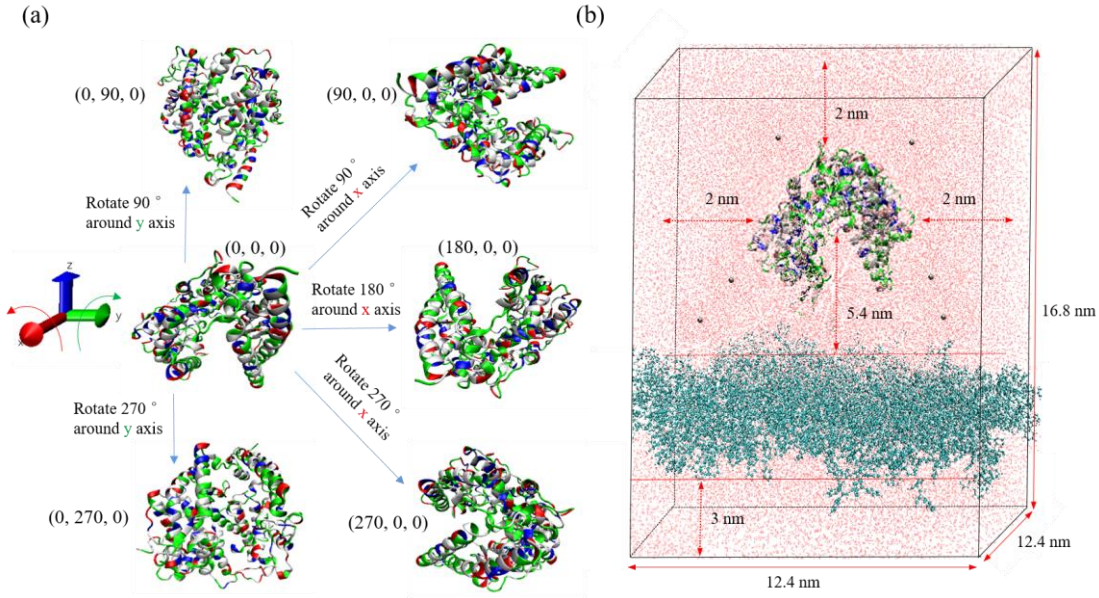

Figure 2. Cubic-orientation settlement of ACE2 immobilized on polystyrene. **(a)** Six initial orientations of ACE2. Different colors represent the properties of amino acids: white is non-polarity, blue is alkaline, red is acidity, and green is polarity; **(b)** The initial structure of ACE2 was to settle on PS, sodium ions are shown in silver.

2.3 Simulation Procedure—cubic-orientation model

As shown in Figure 2a, six initial orientations of ACE2 were to study its proposed settlement on the condensed PS (12.4×12.4×2.0 nm) as predicted in Figure 1d. To easily distinguish each orientation, the cubic coordinates (m, n, 0) are used to represent the different initial orientations of ACE2. Where m and n denote the angles of counterclockwise rotation around x and y axes respectively.

The initial position of ACE2 and PS is shown in Figure 2b. The initial distance between the center of mass of ACE2 and PS assemblers was set to about 5.4 nm. Na^+ was added to neutralize the negative charge of ACE2, without H_2O within 0.3 nm. There are two respective aqueous solutions of 2 and 3 nm layers above ACE2 and PS. In addition, there is a minimum gap of at least 2 nm between ACE2 and simulation boundaries to avoid its mirror image. The aqueous solutions were pH 4.5, 6, 7, 8, 9.5 at 0.15 M NaCl and 0.01, 0.05, 0.1, 0.15, 0.2, 0.25 M NaCl at pH 7.

The interaction of ACE2-PS energy optimization was first to eliminate conformational overlap. And then, both NVT and NPT were performed respectively at 20 and 30 ns to equilibrate. Finally, the statistical information of ACE2 settlement were collected for a 100 ns MD simulation. The PS assemblers as shown in Figure 2b was fixed in Z-axis. The PME (Particle Mesh Ewald) method was used to deal with the long-range electrostatic interaction [65], and the Coulomb and VDW cutoff values are 1.0 nm. The V-rescale method was used to control the temperature [66], and the LINCS algorithm was selected to constrain the bond of the molecule [67]. For solvent water, the single point charge (SPC) model was selected [68]. The simulation time step was 2 fs, and the system trajectory was stored every 10 ps. GROMACS and VMD programs were used to analyze and visualize the simulated trajectory. The number of atoms used in MD simulation is shown in Table S3.

Preprints (www.preprints.org) | NOT PEER-REVIEWED | Posted: 19 May 2023 doi:10.20944/preprints202305.1428.v1

3. Results and Discussion

3.1 Minimum Distance

The interaction of ACE2 and PS was firstly characterized by the minimum separation distance (*d*). The *d* values in Figure 3 are different due to the energy minimization, relaxation, and equilibrium steps during 100 ns simulation. The *d* values were predominately controlled by ACE2 orientations and its circumstances, especially pH. The decrease of *d* indicated that ACE2 had the much favorable attachment towards PS, the critical *d* value was found to be 0.25 nm.

3.1.1 pH Effect

The settlement efficiency of ACE2 in solution towards stationary phase of PS as illustrated in Figure 2b was characterized by counting *d* value ≤ 0.25 nm proportions within 100 ns, representing *N*/10000 fraction (*N*: the number of snapshots with *d* value ≤ 0.25 nm). The total fraction was calculated by the total cubic orientations over 600 ns. There was no significant difference of total fraction as shown in Table 1. The higher one was only 0.662 appeared at pH6, followed by pH 4.5, 9.5, 7, 8 (0.57, 0.56, 0.55, 0.51) in 0.15 M NaCl. As individual fraction above 0.8 bolded in Table 1, it did open a new way to investigate cubic-orientation-settlement mechanism for microfabrication of biochips.

Table 1. Effect of pH on adsorption time fractions of ACE2 evaluated in 0.15 M NaCl.

pH	4.5	6	7	8	9.5
(0, 0, 0)	0.651	**0.798**	0.324	0	0.668
(0, 90, 0)	0.603	**0.941**	**0.962**	**0.844**	**0.970**
(0, 270, 0)	0.560	**0.845**	0.618	**0.829**	0
(90, 0, 0)	**0.880**	0.724	0.060	0.704	**0.892**
(180, 0, 0)	0.532	0.662	**0.813**	0.647	0.347
(270, 0, 0)	0.178	0	0.530	0.006	0.451
Total	0.567	0.662	0.551	0.505	0.555

Both *d* and settlement time of six initial orientations of ACE2 at various pH of 0.15 M NaCl were shown in Figure 3. ACE2 (0, 0, 0) had a relatively fast 19 ns at pH 6, followed by 34 ns at pH 4.5. The adsorption rates of 67 and 56 ns were relatively slow at pH 7 and 9.5, respectively. At pH 9.5, adsorption temporarily occurred at pH 9.5 from 10 to 30 ns. The *d* of pH 8 fluctuated greatly with time, there was no adsorption within 100 ns as indicated as 0 fraction in Table 1. ACE2 (0, 90, 0) had much faster adsorption rates at pH 6, 7, 8 and 9.5, and settled at 6, 3.5, 10.5 and 3 ns, respectively. There was temporary adsorption at pH 4.5 within 10-53 and 75-91 ns time frames. ACE2 (0, 270, 0) had relatively fast adsorption rates of 8.5 and 17 ns at pH 6 and 8, respectively. The adsorption rates were relatively slow at pH 4.5 and 7, appeared approximately at 52 and 45 ns, respectively. ACE2 settlement fluctuated at pH 4.5 and 7 within 15.5-25 and 25-37 ns time frames, respectively. The *d* of pH 9.5 fluctuated greatly within 100 ns. ACE2 (90, 0, 0) had relatively fast adsorption rates of respective 12.5 and 7 ns at pH 4.5 and 9.5, followed by pH 6 and 8, at 23 and 28 ns, respectively. There was a temporary adsorption as occurred at pH 7 from 4 to 12 ns.

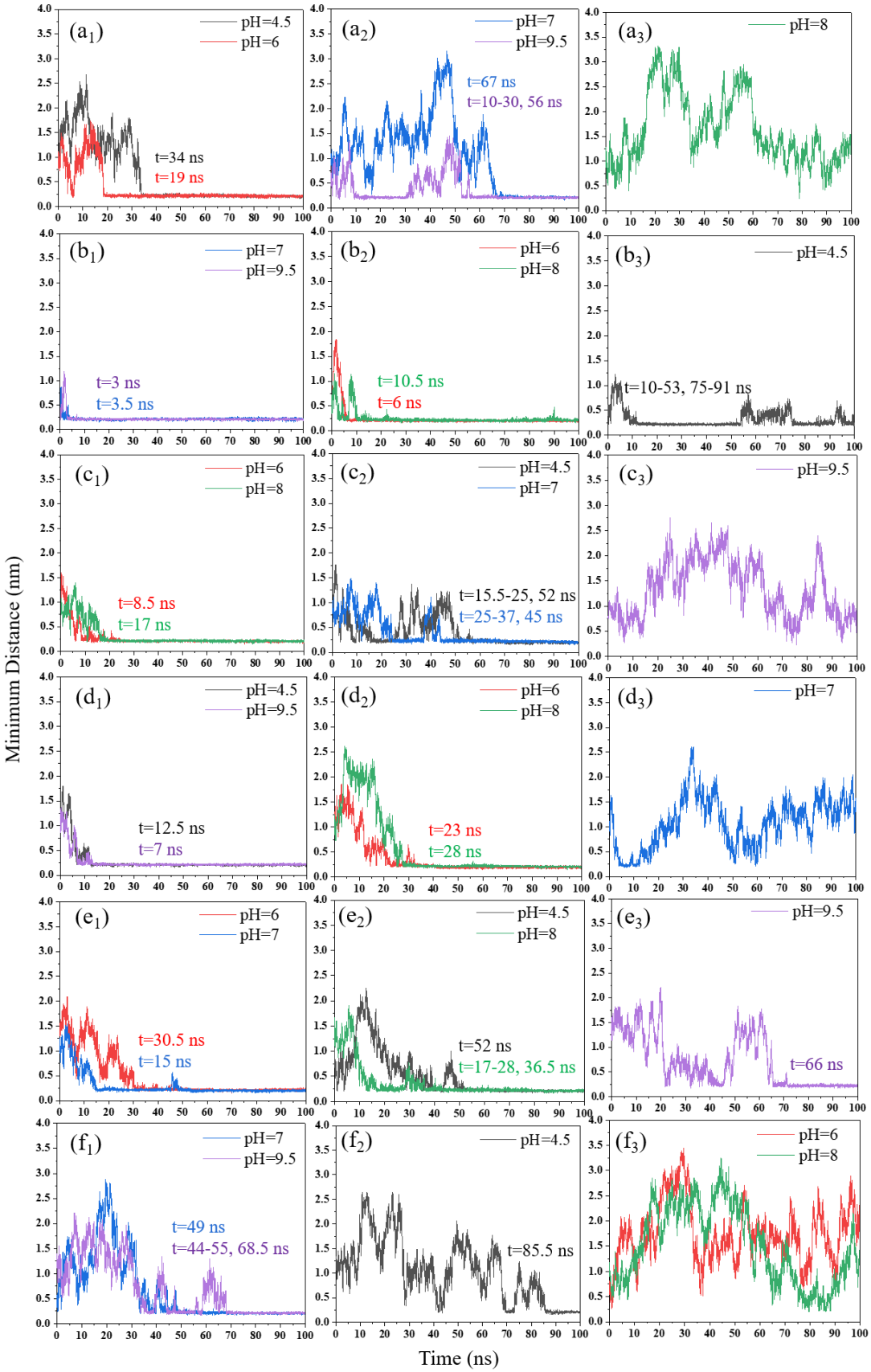

Figure 3. The profile of *d vs* settlement time of ACE2 six initial orientations towards stationary PS under various pH of 0.15M NaCl. Six initial orientations of a Cubic: **(a)** (0, 0, 0); **(b)** (0, 90, 0); **(c)** (0, 270, 0); **(d)** (90, 0, 0); **(e)** (180, 0, 0); **(f)** (270, 0, 0); **1**, **2**, **3** represent pH with relatively fast adsorption rate, followed by reasonable adsorption rate, and no adsorption, respectively.

ACE2 (180, 0, 0) had a relatively fast adsorption rate of 15 ns at pH 7, followed by 30.5 and 36 ns at pH 6 and 8, respectively. The adsorption rate was relatively slow at pH 4.5 and 9.5, it was respective 52 and 66 ns. There was *d* fluctuation from 17 to 28 ns at pH 8. ACE2 (270, 0, 0) had the slower adsorption rates of 85.5, 49 and 68.5 ns at pH 4.5, 7 and 9.5, respectively. There was temporary adsorption from 44 to 55 ns at pH 9.5. The *d* of pH 6 and 8 fluctuated greatly within 100 ns. Therefore, ACE2 (0, 90, 0) initial orientation at pH 6, 7, 8, 9.5 is much more favorable settlement towards PS, while (270, 0, 0) orientation is not ideal in 0.15 M NaCl.

3.1.2 NaCl Effect

The individual and total fractions of ACE2 six initial orientations in Table 2 were characterized and calculated as the same methodology as discussed in Section 3.1.1. Regarding total fractions, 0.15 M NaCl was optimum (i.e., 0.55) solution, while 0.01 M NaCl was only 0.14. The ionic strength could have an important influence on the interaction of ACE2 and PS. The immobilization of ACE2 was increased and then declined with increasing NaCl.

Table 2. Effect of NaCl on adsorption time fractions of ACE2 evaluated at pH 7

NaCl (M)	0.01 M	0.05 M	0.1 M	0.15 M	0.2 M	0.25
（0, 0, 0）	0.017	0.002	0.984	0.324	0.043	0
（0, 90, 0）	0.001	0.867	0	0.962	0.949	0.904
（0, 270, 0）	0.298	0.906	0.209	0.618	0.014	0.489
（90, 0, 0）	0.322	0.068	0.904	0.060	0.877	0.208
（180, 0, 0）	0.088	0.670	0.166	0.813	0.123	0.059
（270, 0, 0）	0.095	0.118	0.327	0.530	0.402	0.362
Total	0.137	0.439	0.432	0.551	0.401	0.337

As shown in Figure 4, ACE2 settlement time on stationary PS was characterized by various NaCl concentrations at pH 7. ACE2 (0, 0, 0) had just 1 ns settled on PS in 0.1 M NaCl, its adsorption rate was relatively slow and fluctuated till 67 ns in 0.15 M NaCl. There was temporary adsorption of ACE2 within 4.5-10 ns time frame in both 0.2 and 0.25 M NaCl. The *d* of 0.01, 0.05, 0.25 M NaCl fluctuated greatly, there was no settlement at all. ACE2 (0, 90, 0) had a relatively fast adsorption rate in high NaCl concentration, respectively settled at 9, 3.5, 5.5 and 10 ns, except in 0.01 or 0.1 M NaCl solution. ACE2 (0, 270, 0) had a relatively fast adsorption 10 ns rate in 0.05 M NaCl, the rest was relatively slow at 73, 78, 45 and 57 ns, respectively. There was although temporary adsorption in 0.15 M NaCl within 25-37 ns, the *d* fluctuated greatly in 0.2 M NaCl. ACE2 (90, 0, 0) had a relatively fast adsorption 13 ns rate in 0.2 M NaCl, followed by 22 ns in 0.1 M NaCl. The adsorption rate of 0.01 M NaCl was relatively slow at 69 ns. There was almost temporary adsorption occurred, such as 0.05, 0.1, 0.15, 0.25 M NaCl within 68-74 and 79-84, 5-18, 4-12, 71.5-95 ns, respectively. ACE2 (180, 0, 0) had a reasonable adsorption 15 ns rate in 0.15 M NaCl, followed by 35.5 ns in 0.05 M NaCl. The immobilization of ACE2 was relatively slow in low and high concentrations, such as respective 0.01, 0.1 and 0.2 M NaCl at 93.5, 84.5 and 88 ns. The *d* of 0.25 M NaCl fluctuated greatly, there was no sign of immobilization. The immobilization of ACE2 (270, 0, 0) in 0.05, 0.15 and 0.2 M NaCl was only triggered at 89, 49 and 57.5 ns, respectively. There was temporary adsorption occurred in 0.1, 0.25 M NaCl within 8.5-20 and 29-46, 28.5-40 ns time frames, respectively. There was no immobilization in lower 0.01 M NaCl concentration. Therefore, ACE2 (0, 90, 0) initial orientation has effective immobilization, while (0, 0, 0) was almost none.

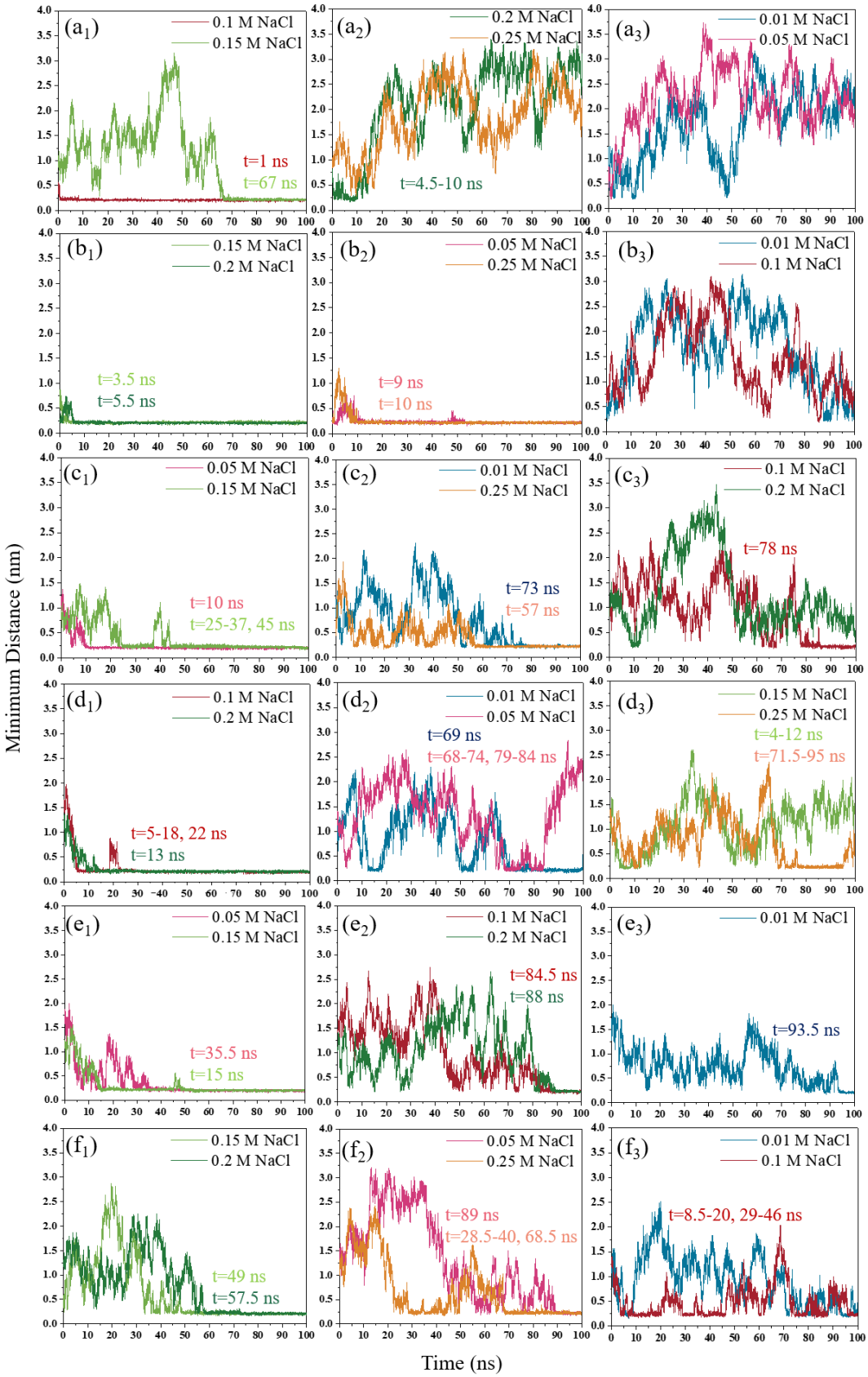

Figure 4. The profile of *d vs* settlement time of ACE2 six initial orientations towards stationary PS in NaCl solution at pH 7: Six initial orientations of a Cubic: **(a)** (0, 0, 0); **(b)** (0, 90, 0); **(c)** (0, 270, 0); **(d)** (90, 0, 0); **(e)** (180, 0, 0); **(f)** (270, 0, 0); **1**, **2**, **3** represent NaCl concentrations with relatively fast adsorption rate, followed by reasonable adsorption rate, and no adsorption, respectively.

3.2 Interaction Energy

The interaction energy is becoming more and more popular in explaining the adsorption between membrane and protein [69-71]. The VDW interaction energy and electrostatic interaction energy of proteins with six initial orientations proposed were investigated to quantitate interaction between ACE2 and PS.

3.2.1 pH Effect

The interaction energy of six ACE2 initial orientations and PS was characterized by the effect of pH in 0.15 M NaCl as shown Figure 5. The total interaction energy of ACE2 (0, 0, 0) at pH 8 was higher, almost no adsorption with PS. The unstable total interaction energy finally ranging from -200 to -300 KJ/mol at pH 4.5, 6, 7 and 9.5 was mainly attributed to VDW. The total interaction energy of ACE2 (0, 90, 0) with PS at pH 6 was relatively stable at -250 KJ/mol dominated by VDW, while the others were unstable and fluctuated except pH 9.5 only with 20 ns. ACE2 (0, 270, 0) at pH 9.5 had almost no adsorption, the total interaction energy of the others was continuously negative, especially -350 KJ/mol at pH 6. Both initial orientations (0, 90, 0) and (0, 270, 0) of ACE2 at pH 6 were in a similar situation dominated by VDW. ACE2 (90, 0, 0) at pH 7 had almost no adsorption, the rest of total interaction energy was continuously negative. Especially, the total interaction energy of ACE2 (90, 0, 0) had stable -350 KJ/mol reached by respective VDW and electrostatic interactions at pH 6 and 9.5. ACE2 (180, 0, 0) showed a continuous negative total interaction energy, the maximum -450 KJ/mol dominated by VDW was reached at pH 7. ACE2 (270, 0, 0) at pH 7 also showed a relatively stable interaction of -250 KJ/mol with PS by mainly VDW. Interesting, there was almost no adsorption with PS at pH 6 and 8, except subtle adsorption at both pH 4.5 and 9.5.

The interaction energy is dominated by VDW, while initial orientation (90, 0, 0) is contributed by both VDW and electrostatic interactions, especially equaled as -150 KJ/mol at pH 9.5.

3.2.2 NaCl Effect

The interaction energy of six ACE2 initial orientations and PS was characterized by the effect of NaCl at pH 7 as shown Figure 6. ACE2 (0, 0, 0) in 0.1 and 0.15 M NaCl had appropriate immobilization, and respectively reached -300 and -250 KJ/mol attributed by both VDW and electrostatic interactions. The rest of the high and low NaCl concentration was almost no immobilization of ACE2 on PS. The total interaction energy of ACE2 (0, 90, 0) in 0.2 M NaCl reached -400 KJ/mol, attributed by both -300 KJ/mol VDW and -100 KJ/mol electrostatic interactions. There was almost no immobilization in 0.01 and 0.1 M NaCl, except for 0.05, 0.15, and 0.25 M NaCl with subtle interaction energy from -100 to -150 KJ/mol. ACE2 (0, 270, 0) in 0.2 M NaCl had almost no immobilization, nevertheless total interaction energy of ACE2 immobilized in the rest of NaCl was from -100 to -350 KJ/mol. The total interaction energy of ACE2 (90, 0, 0) in 0.1 and 0.2M NaCl reached -300 and -200 KJ/mol, respectively. ACE2 (90, 0, 0) in 0.01 M NaCl interestingly had -100 KJ/mol total interaction energy, there was almost no immobilization in the rest of NaCl solution. ACE2 (180, 0, 0) in all kinds of NaCl immobilized on PS, except in 0.25 M NaCl. Total interaction energy reached up to -450 KJ/mol in 0.15 M NaCl, due to -350 KJ/mol contribution from VDW. Like ACE2 (90, 0, 0), the low concentration of 0.05 M NaCl also attributed -400 KJ/mol total interaction energy. However, there was almost no ACE2 (270, 0, 0) immobilization in low NaCl concentrations such as 0.01 and 0.05 M NaCl. ACE2 (270, 0, 0) in high NaCl concentrations greater than 0.1 M NaCl showed subtle values of total interaction energy ranging from -100 to -250 KJ/mol, mainly attributed to the low interaction energy of VDW and electrostatic interaction.

The VDW interaction dominates ACE2 immobilization, especially two scenarios of ACE2 (180, 0, 0) in 0.15 M NaCl and ACE2 (0, 90, 0) in 0.2 M NaCl, respectively -350 KJ/mol VDW *vs* -450 KJ/mol total and -300 KJ/mol VDW *vs* -400 KJ/mol total. There will be speculation that specific immobilization in lower concentrations, such as ACE2 (180, 0, 0) with -400 KJ/mol in 0.05 M NaCl, and ACE2 (90, 0, 0) with -100 KJ/mol in 0.01 M NaCl.

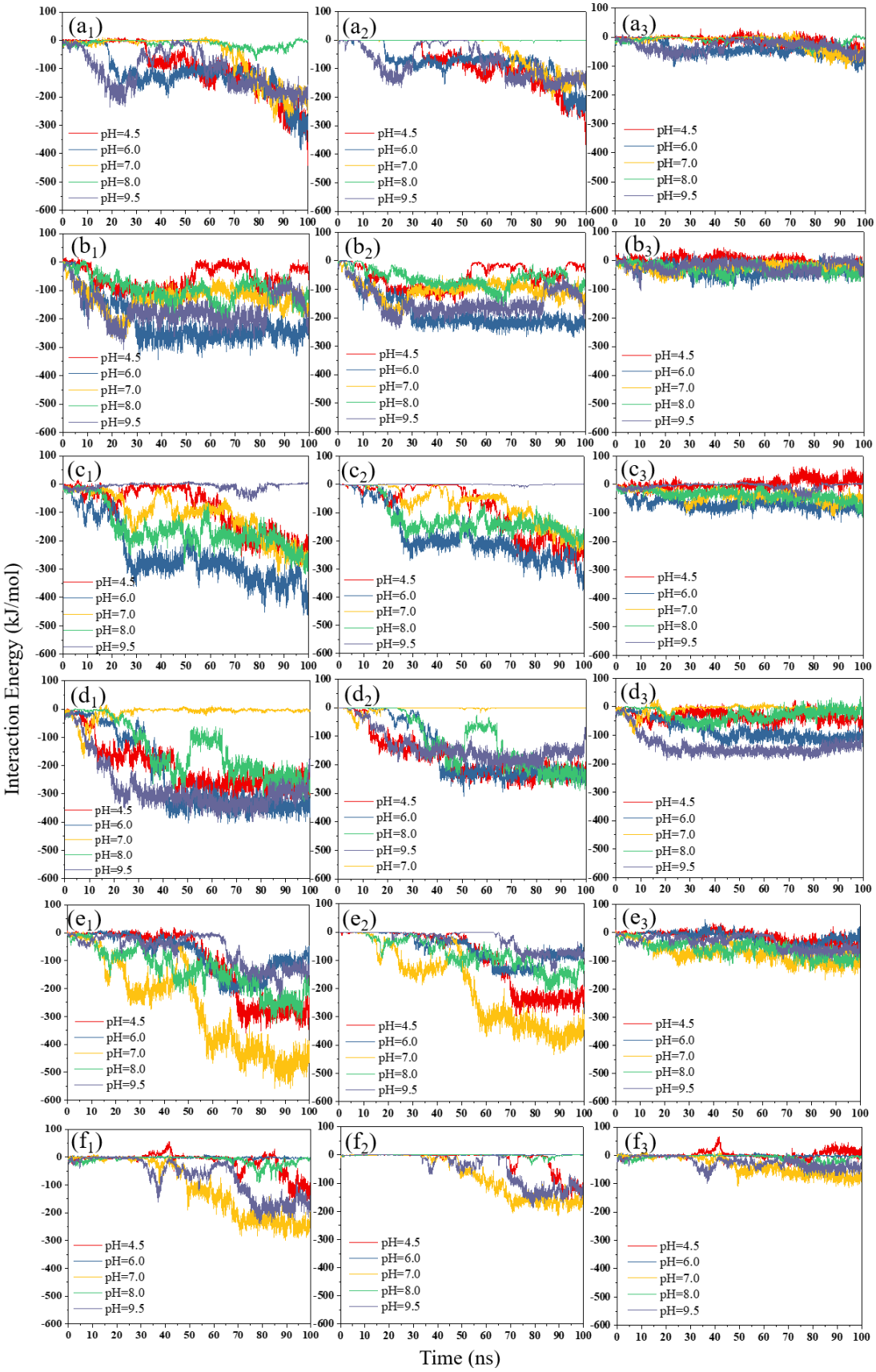

Figure 5. Effect of pH on the interaction energy of ACE2 six initial orientations with PS in 0.15 M NaCl. Six initial orientations of a Cubic: **(a)** (0, 0, 0); **(b)** (0, 90, 0); **(c)** (0, 270, 0); **(d)** (90, 0, 0); **(e)** (180, 0, 0); **(f)** (270, 0, 0); **1**, **2**, **3** represent the total, VDW, electrostatic interaction energy, respectively.

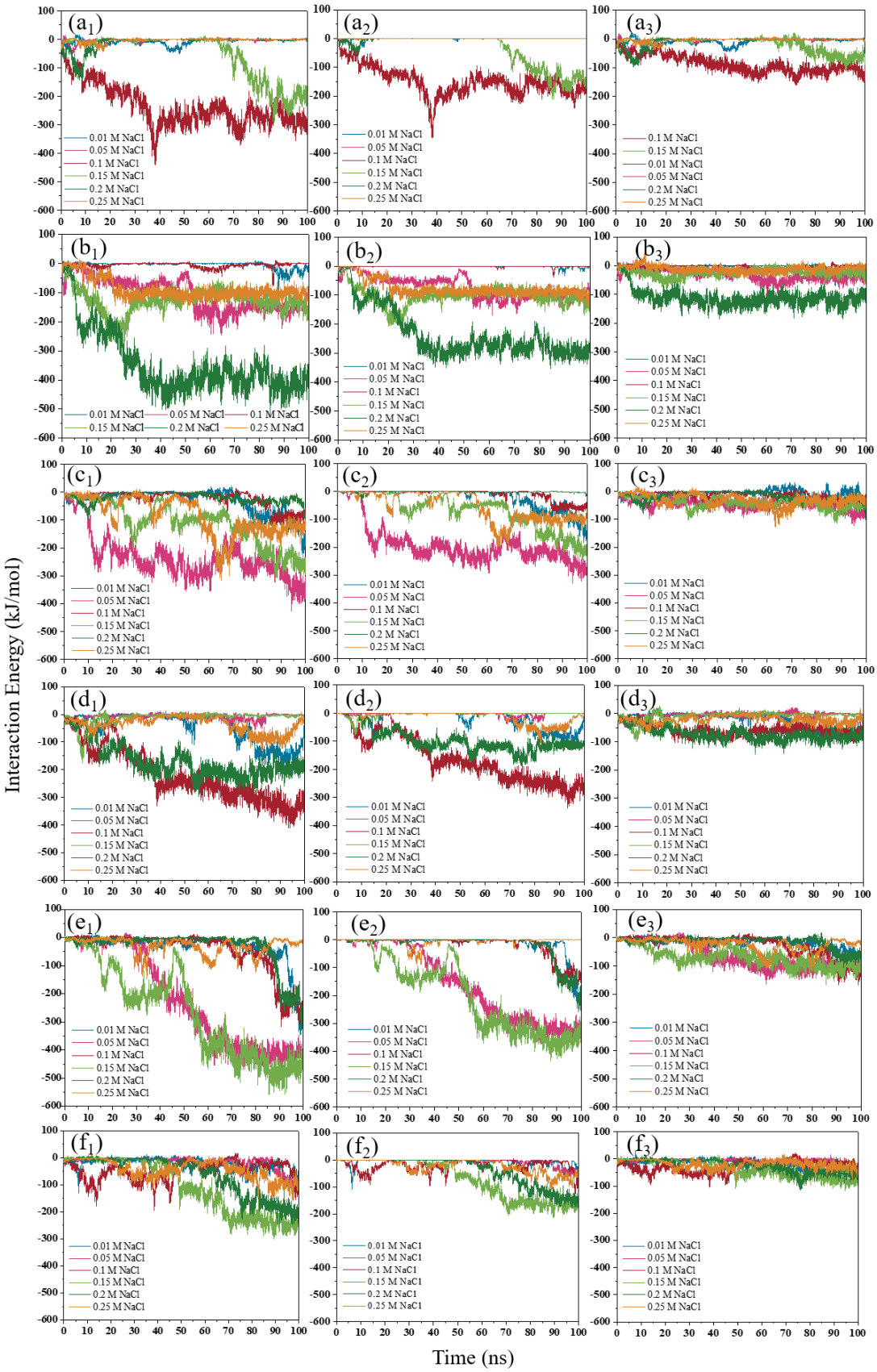

Figure 6. Effect of NaCl on the interaction energy of ACE2 six initial orientations with PS at pH 7. Six initial orientations of a Cubic: **(a)** (0, 0, 0); **(b)** (0, 90, 0); **(c)** (0, 270, 0); **(d)** (90, 0, 0); **(e)** (180, 0, 0); **(f)** (270, 0, 0); **1**, **2**, **3** represent the total, VDW, electrostatic interaction energy, respectively.

Preprints (www.preprints.org) | NOT PEER-REVIEWED | Posted: 19 May 2023 doi:10.20944/preprints202305.1428.v1

3.3 Adsorption Behavior

The parameters characterizing the adsorption behavior of ACE2 on PS surface at various pH (4.5, 6, 7, 8, 9.5) of 0.15 M NaCl were shown in Table S4. The overall configuration and stability of ACE2 were measured by calculating the root mean square deviation (RMSD) of ACE2 C-alpha relative to the initial structure and the radius gyration (Rg) of the protein. ACE2 immobilization on PS was captured in 0.15 M NaCl, as shown in Figure 7. As tabulation illustrated, there were favorable initial orientations quantified by settlement time, interaction energy level and ACE2 Rg, due to relatively fast, substantial bonding and stable configuration. It will provide instructive information to possibly immobilize ACE2 in 0.15 M NaCl.

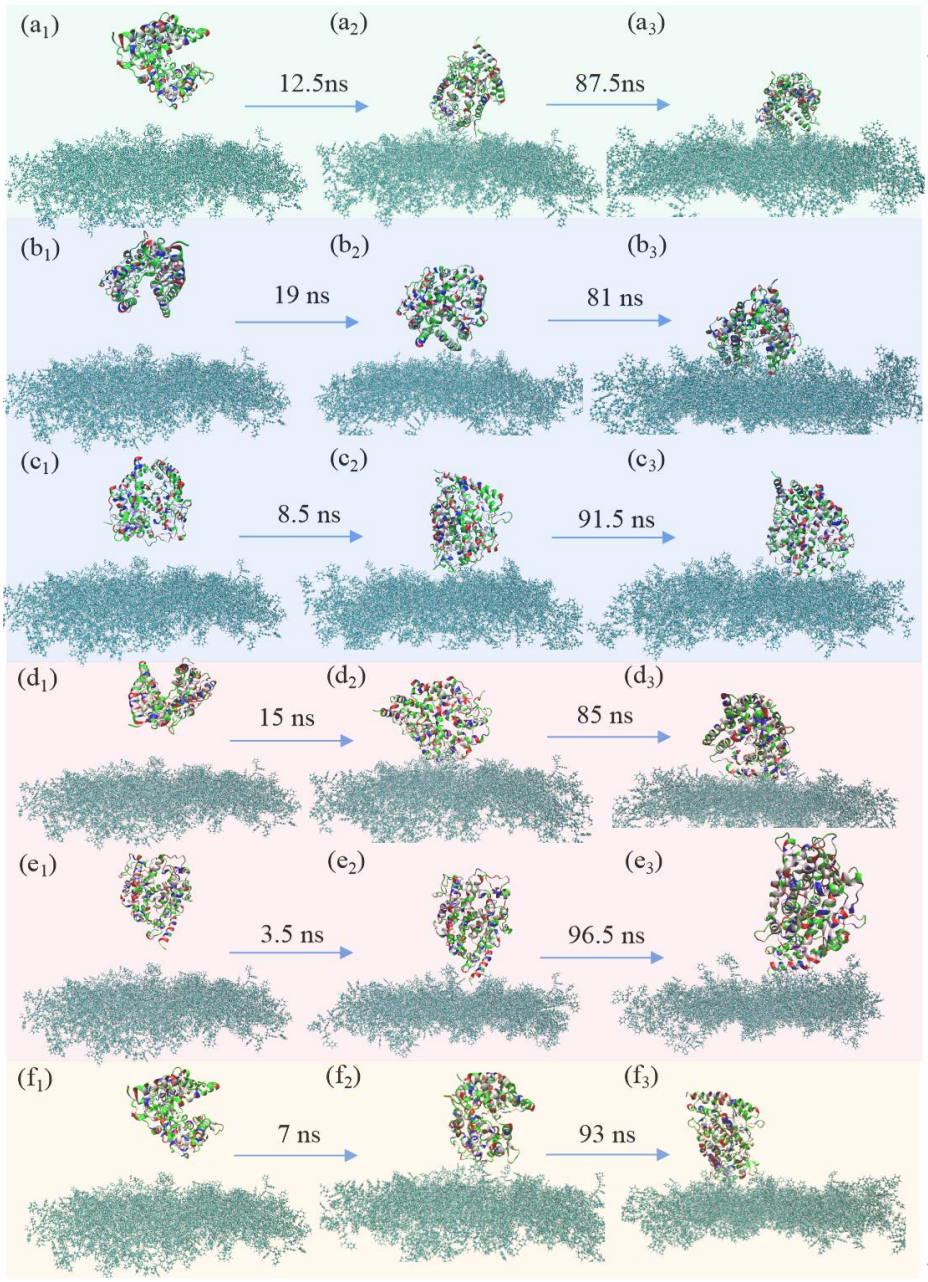

VDW/ Electrostatic (KJ/mol)	RMSD/ Rg (nm)
-216.3/ -40.0	0.25/ 2.51
-216.7/ -76.6	0.22/ 2.50
-292.0/ -79.2	0.22/ 2.49
-350.5/ -100.9	0.27/ 2.48
-119.3/ -26.2	0.27/ 2.48
-143.2/ -129.2	0.26/ 2.50

Figure 7. The immobilization of ACE2 on PS under the optimal conditions of 0.15 M NaCl. **(a)** pH 4.5 (90, 0, 0); **(b)** pH 6 (0, 0, 0); **(c)** pH 6 (0, 270, 0); **(d)** pH 7 (180, 0, 0); **(e)** pH 7 (0, 90, 0); **(f)** pH 9.5 (90, 0, 0). **1**, **2**, **3** represent the initial, start and final state, respectively. The energy and RMSD/Rg were averaged at the last 5 ns.

Preprints (www.preprints.org) | NOT PEER-REVIEWED | Posted: 19 May 2023 doi:10.20944/preprints202305.1428.v1

The parameters characterizing the adsorption behavior of ACE2 on PS surface at various NaCl concentrations (0.01, 0.05, 0.1, 0.15, 0.2, 0.25 M) at pH 7 were shown in Table S5. ACE2 immobilization on PS was captured at pH 7, as shown in Figure 8. As tabulation illustrated similarly as Figure 7, favorable initial orientations were summarized by quantitative settlement time, interaction energy level and ACE2 Rg. It will provide an instructive way to possibly immobilize ACE2 at pH 7, based on its relatively fast, substantial bonding and stable configuration.

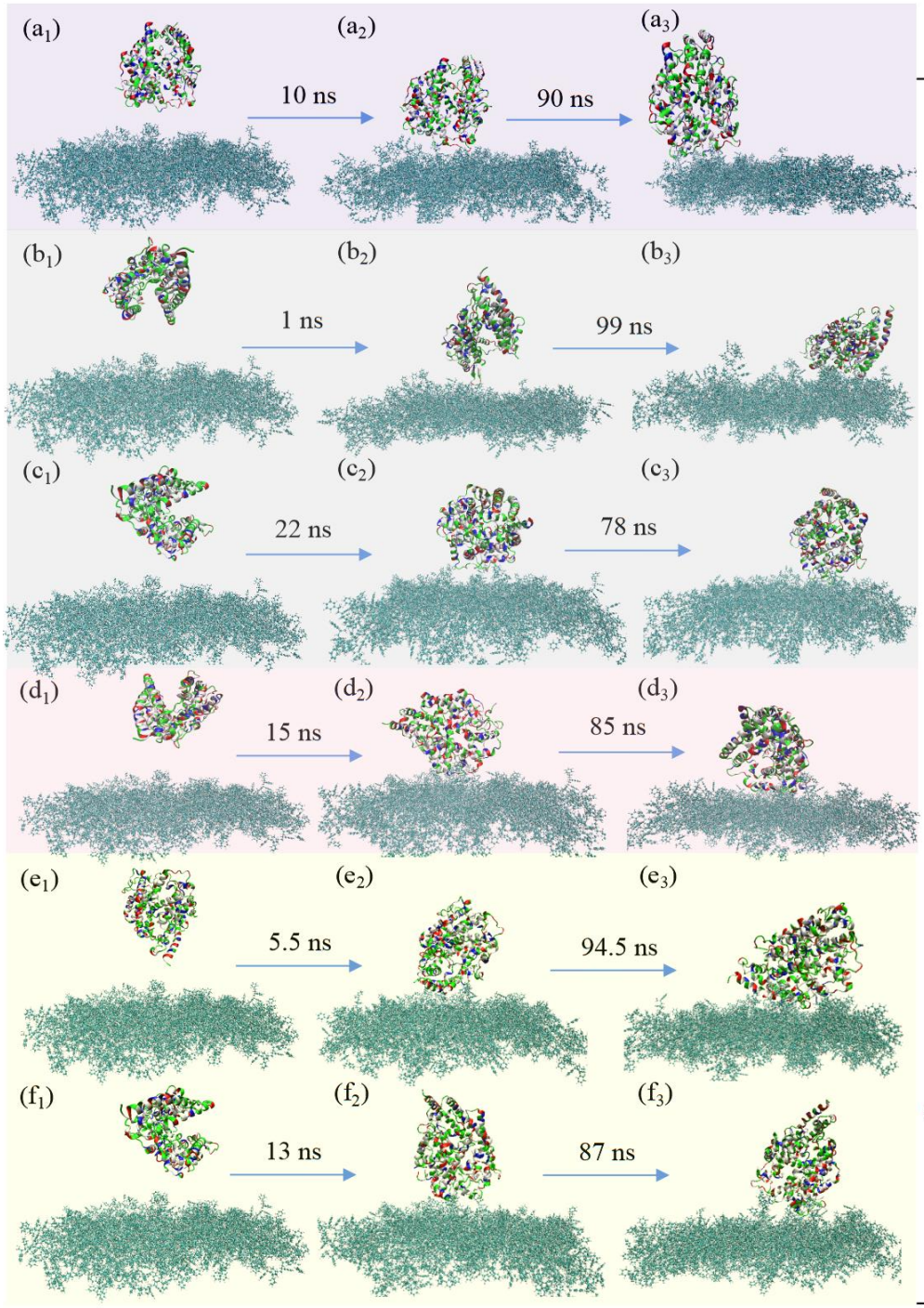

VDW/ Electrostatic (KJ/mol)	RMSD/ Rg (nm)
-273.9/ -74.7	0.26/ 2.46
-178.6/ -112.9	0.27/ 2.47
-264.4/ -70.8	0.26/ 2.50
-350.5/ -100.9	0.27/ 2.48
-295.5/ -110.5	0.23/ 2.49
-113.1/ -78.4	0.24/ 2.48

Figure 8. The immobilization of ACE2 on PS under the optimal conditions of pH 7. **(a)** 0.05 M NaCl (0, 270, 0); **(b)** 0.1 M NaCl (0, 0, 0); **(c)** 0.1 M NaCl (90, 0, 0); **(d)** 0.15 M NaCl (180, 0, 0); **(e)** 0.2 M NaCl (0, 90, 0); **(f)** 0.2 M NaCl (90, 0, 0). **1**, **2**, **3** represent the initial, start and final state, respectively. The energy and RMSD/Rg were averaged at the last 5 ns.

4. Conclusions

The immobilization of ACE2 on polymer is conducive to the development of real-time and *in-situ* diagnostic SARS-CoV-2 biochips. A cubic-orientation settlement mode was successfully proposed for ACE2 immobilization. The adsorption behaviors of ACE2 initial orientations on PS was studied using MD simulation at ambient temperature, by optimizing pH and NaCl parameters. The results evidenced that the VDW interaction energy dominates substantial bonding between ACE2 and PS. The adsorption rate of ACE2 in 0.15 M NaCl preferred pH 4.5 and 9.5 for (90, 0, 0), while pH 6, 7 for (0, 0, 0) and (0, 270, 0), (180, 0, 0) and (0, 90, 0), respectively. At pH 7 ambient temperature, ACE2 in 0.05, 0.1, 0.2 M NaCl respectively preferred (0, 270, 0), (0, 0, 0) and (90, 0, 0), (0, 90, 0) and (90, 0, 0) initial orientations, due to relatively fast, substantial bonding and stable configuration. It will provide a new conducive way to optimize suitable curing protein conditions.

Supplementary Materials: The following supporting information can be downloaded at the website of this paper posted on Preprints.org., Table S1: Number of amino acid residues in ACE2; Table S2: Total charge of ACE2 under different conditions; Table S3: The number of atoms used in MD simulation; Table S4: Parameters characterizing the adsorption behavior of ACE2 on PS surface at different pH values of 0.15 M NaCl, energy and RMSD/Rg were averaged in the last 5 ns; Table S5: Parameters characterizing the adsorption behavior of ACE2 on PS surface with different NaCl concentrations, energy and RMSD/Rg were averaged in the last 5 ns.

Author Contributions: Conceptualization, Y.J.Y.; methodology, Y.M. and Y.J.Y.; validation, Y.M. and Y.J.Y; formal analysis, Y.M. and Y.J.Y; investigation, Y.M. and Y.J.Y; writing—original draft preparation, Y.M.; writing—review and editing, Y.J.Y.; supervision, Y.J.Y.; project administration, Y.J.Y.; funding acquisition, Y.J.Y. All authors have read and agreed to the published version of the manuscript.

Funding: This research was funded by National Natural Science Foundation of China, RFIS 2231101354. The APC was funded by MDPI Biosensors.

Institutional Review Board Statement: Not applicable.

Informed Consent Statement: Not applicable.

Conflicts of Interest: The authors declare no conflict of interest.

References

1. Ullah, I.; Wang, W.W.; Ma, N.; Lendlein, A. Multiblock copolymers type PDC - A family of multifunctional biomaterials for regenerative medicine1. *Clin. Hemorheol. Microcirc.* **2022**, *80*, 327–341.
2. Yu, Y.Y.; Ghalandari, B.; Shen, G.X.; Wang, L.P.; Liu, X.; Wang, A.T.; Li, S.J.; Xie, H.Y.; Ding, X.T. Poly (N-vinylpyrrolidone) modification mitigates plasma protein corona formation on phosphomolybdate-based nanoparticles. *J. Nanobiotechnology.* **2021**, *19*, 445.
3. Chen, Z. Surface Hydration and antifouling activity of zwitterionic polymers. *Langmuir* **2022**, *38*, 4483–4489.
4. Ma, Z.Z.; Sun, J.; Dong, X.H.; Gan, D.L.; Peng, W.; Li, Y.X.; Qian, W.J.; Liu, P.S.; Shen, J. Zwitterionic/active ester block polymers as multifunctional coatings for polyurethane-based substrates. *J. Mater. Chem. B.* **2022**, *10*, 3687–3695.
5. Yeh, S.L.; Deval, P.; Wu, J.G.; Luo, S.C.; Tsai, W.B. One-step electrochemical deposition of antifouling polymers with pyrogallol for biosensing applications. *J. Mater. Chem. B.* **2022**, *10*, 2504–2511.
6. Kilic, T.; Gessner, I.; Cho, Y.K.; Jeong, N.; Quintana, J.; Weissleder, R.; Lee, H. Zwitterionic polymer electroplating facilitates the preparation of electrode surfaces for biosensing. *Adv. Mater.* **2022**, *34*, 2107892.
7. Badoux, M.; Billing, M.; Klok, H. Polymer brush interfaces for protein biosensing prepared by surface-initiated controlled radical polymerization. *Polym. Chem.* **2019**, *1*, 2925–2951.
8. Mierczynska-Vasilev, A.; Smith, P. Adsorption of wine constituents on functionalized surfaces. *Molecules* **2016**, *21*, 1394.
9. Galus, S.; Lenart, A. Optical, mechanical, and moisture sorption properties of whey protein edible films. *J Food Process Eng*, **2019**, *42*, e13245.
10. Tatikonda, A. K.; Tkachev, M.; Naaman, R. A highly sensitive hybrid organic–inorganic sensor for continuous monitoring of hemoglobin. *Biosens. Bioelectron.* **2013**, *45*, 201–205.

11. Köllnberger, A.; Schrader, R.; Briehn, C.A. Carboxylic acid mediated antimicrobial activity of silicone elastomers. *Mater. Sci. Eng. C* **2020**, *113*, 111001.
12. Wang, K.; Arado, T.; Huner, A.; Seol, H.; Liu, X.; Wang, H.F.; Hassan, L.; Suresh, K.; Kim, S.; Cheng, G. Thermoplastic zwitterionic elastomer with critical antifouling properties. *Biomater. Sci.* **2022**, *10*, 2892–2906.
13. Namekawa, K.; Tokoro Schreiber, M.; Aoyagi, T.; Ebara, M. Fabrication of zeolite–polymer composite nanofibers for removal of uremic toxins from kidney failure patients. *Biomater. Sci.* **2014**, *2*, 674.
14. Xu, Z.L.; Yuan, Y.J. Implementation of guiding layers of surface acoustic wave devices: A review. *Biosens. Bioelectron.* **2018**, *99*, 500-512.
15. Ozboyaci, M.; Kokh, D.B.; Corni, S.; Wade, R.C. Modeling and simulation of protein-surface interactions: achievements and challenges. *Q. Rev. Biophys.* **2016**, *49*, 1–45.
16. Gibson, C.C.; Puleo, D.A.; Bizios, R. *Biological interactions on materials surfaces : understanding and controlling protein, cell, and tissue responses*; Springer: New York, USA, 2009; pp. 1–17.
17. Ang, W.S.; Elimelech, M. Protein (BSA) fouling of reverse osmosis membranes: Implications for wastewater reclamation. *J. Membr. Sci.* **2007**, *296*, 83–92.
18. Dee, K.C.; Puleo, D.A.; Bizios, R. *An introduction to tissue-biomaterial interactions*; John Wiley & Sons: New York, USA, 2003; pp. 37–52.
19. Wang, K.; Zhou, C.; Hong, Y.; Zhang, X. A review of protein adsorption on bioceramics. *Interface Focus* **2012**, *2*, 259–277.
20. Noh, H.; Vogler, E.A. Volumetric interpretation of protein adsorption: Competition from mixtures and the Vroman effect. *Biomaterials* **2007**, *28*, 405–422.
21. Hirsh, S.L.; McKenzie, D.R.; Nosworthy, N.J.; Denman, J.A.; Sezerman, O.U.; Bilek, M.M.M. The Vroman effect: Competitive protein exchange with dynamic multilayer protein aggregates. *Colloids Surf. B* **2013**, *103*, 395–404.
22. Ratner, B.D.; Hoffman, A.S.; Schoen, F.J.; Lemons, J.E. *Biomaterials science: An introduction to materials in medicine*; Elsevier Academic Press: San Diego, USA, 2004; pp.237–246.
23. Tizazu, G. Investigation of the effect of molecular weight, density, and initiator structure size on the repulsive force between a PNIPAM polymer brush and protein. *Adv. Polym. Technol.* **2022**, *2022*, 1–20.
24. Jönsson, M.; Johansson, H. Effect of surface grafted polymers on the adsorption of different model proteins. *Colloids Surf. B* **2004**, *37*, 71–81.
25. Jin, Z.; Feng, W.; Beisser, K.; Sheardown, H.; Brash, J.L. Protein-resistant polyurethane prepared by surface-initiated atom transfer radical graft polymerization (ATRgP) of water-soluble polymers: Effects of main chain and side chain lengths of grafts. *Colloids Surf. B* **2009**, *70*, 53–59.
26. Akkas, T.; Citak, C.; Sirkecioglu, A.; Güner, F.S. Which is more effective for protein adsorption: surface roughness, surface wettability or swelling? Case study of polyurethane films prepared from castor oil and poly(ethylene glycol). *Polym. Int.* **2013**, *62*, 1202–1209.
27. Zhang, Z.H.; Li, G.J.; Yan, F.F.; Zheng, X.J.; Li, X.L. Towards understanding of protein adsorption behavior on plasma polymerized pyrrole film. *Cent. Eur. J. Chem.* **2012**, *10*, 1157–1164.
28. Molino, P.J.; Higgins, M.J.; Innis, P.C.; Kapsa, R.M.I.; Wallace, G.G. Fibronectin and bovine serum albumin adsorption and conformational dynamics on inherently conducting polymers: a QCM-D study. *Langmuir* **2012**, *28*, 8433–8445.
29. Takami, K.; Matsuno, R.; Ishihara, K. Synthesis of polyurethanes by polyaddition using diol compounds with methacrylate-derived functional groups. *Polymer* **2011**, *52*, 5445–5451.
30. Zhang, Z.; Feng, C. The investigation of protein adsorption behaviors on different functionalized polymers films. *J. Biotechnol.* **2007**, *2*, 743–751.
31. Bunk, J.K.G.; Pospiech,D.U.; Eichhorn, K.; Müller, M.; Werner, C.; Bellmann, C.; Simon, F.; Pleul, D.; Grundke, K. Studying the influence of chemical structure on the surface properties of polymer films. *Colloids Surf. A* **2010**, *362*, 47–57.
32. Oscarsson, S. Factors affecting protein interaction at sorbent interfaces. *J. Chromatogr. B* **1997**, *699*, 117–131.
33. Mo, H.; Tay, K.G.; Ng, H.Y. Fouling of reverse osmosis membrane by protein (BSA): Effects of pH, calcium, magnesium, ionic strength and temperature. *J. Membr. Sci.* **2008**, *315*, 28–35.
34. Wang, Y.; Tang, C.Y. Protein fouling of nanofiltration, reverse osmosis, and ultrafiltration membranes—The role of hydrodynamic conditions, solution chemistry, and membrane properties. *J. Membr. Sci.* **2011**, *376*, 275–282.
35. She, Q.; Tang, C.Y.; Wang, Y.; Zhang, Z.J. The role of hydrodynamic conditions and solution chemistry on protein fouling during ultrafiltration. *Desalination* **2009**, *249*, 1079–1087.

36. Li, W.; Cao, F.; He, C.; Ohno, K.; Ngai, T. Measuring the interactions between protein-coated microspheres and polymer brushes in aqueous solutions. *Langmuir* **2018**, *34*, 8798–8806.
37. Wang, B.; Shi, B. Comparison of surface tension components and hansen solubility parameters theories. part I: explanation of protein adsorption on polymers. *J. Macromol. Sci., Phys.* **2010**, 49, 383–391.
38. Sadegh, H.; Sahay, R.; Soni, S. Protein–polymer interaction: Transfer loading at interfacial region of PES-based membrane and BSA. *J. Appl. Polym. Sci.* **2019**, *136*, 47931.
39. Kim, J.T.; Shin, G.H. Adsorption behavior of β-lactoglobulin onto polyethersulfone membrane surface. *J. Adhes. Sci. Technol.* **2015**, *29*, 2245–2255.
40. Prozeller, D.; Rosenauer, C.; Morsbach, S.; Landfester, K. Immunoglobulins on the surface of differently charged polymer nanoparticles. *Biointerphases* **2020**, *15*, 31009.
41. Moringo, N.A.; Shen, H.; Tauzin, L.J.; Wang, W.X.; Landes, C.F. Polymer free volume effects on protein dynamics in polystyrene revealed by single-molecule spectroscopy. *Langmuir* **2020**, *36*, 2330–2338.
42. He, C.; Zhang, H.; Lin, C.; Wang, L.; Yuan, S.L. A molecular dynamics study on the adsorption of a mussel protein on two different films: Polymer film and a SAM. Chem. *Phys. Lett.* **2017**, *676*, 144–149.
43. Panos, M.; Sen, T.Z.; Ahunbay, M.G. Molecular simulation of fibronectin adsorption onto polyurethane surfaces. *Langmuir* **2012**, *28*, 12619–12628.
44. Li, B.; Jain, P.; Ma, J.; Smith, J.K.; Yuan, Z.; Hung, H.C.; He, Y.; Lin, X.; Wu, K.; Pfaendtner, J.; Jiang, S. Trimethylamine N-oxide-derived zwitterionic polymers: A new class of ultralow fouling bioinspired materials. *Sci. Adv.* **2019**, *5*, w9562.
45. Mollahosseini, A.; Saadati, S.; Abdelrasoul, A. Effects of mussel-inspired co-deposition of 2-hydroxymethyl methacrylate and poly (2-methoxyethyl acrylate) on the hydrophilicity and binding tendency of common hemodialysis membranes: Molecular dynamics simulations and molecular docking studies. *J. Comput. Chem.* **2022**, *43*, 57–73.
46. Ghermezcheshme, H.; Mohseni, M.; Ebrahimi, M.; Makki, H.; Martinelli, E.; Braccini, S.; Galli, G. Effect of network topology on the protein adsorption behavior of hydrophilic polymeric coatings. *ACS Appl. Polym. Mater.* **2022**, *4*, 129–140.
47. Hirst, E.R.; Xu, W.L.; Bronlund, J.E.; Yuan, Y.J. Surface Acoustic Wave Delay Line for Bond Rupture Biosensors. *IEEE Sensors J.* **2011**, *11*, 2952-2956.
48. Xu, Z.L.; Yuan, Y.J. Quantification of Staphylococcus aureus by ZnO naonparticles-based surface acoustic wave. *RSC Adv.* **2019**, *9*, 8411-8414.
49. Astuti, I.; Ysrafil. Severe acute respiratory syndrome coronavirus 2 (SARS-CoV-2): An overview of viral structure and host response. *Diabetes Metab. Res. Rev.* **2020**, *14*, 407–412.
50. Cordes, A.K.; Rehrauer, W.M.; Accola, M.A.; Wolk, B.; Hilfrich, B.; Heim, A. Fully automated detection and differentiation of pandemic and endemic coronaviruses (NL63, 229E, HKU1, OC43 and SARS-CoV-2) on the hologic panther fusion. *J. Med. Virol.* **2021**, *93*, 4438–4445.
51. Neese, F. Software update: The ORCA program system—Version 5.0. *WIREs Comput Mol Sci.* **2022**, *12*, e1606.
52. Grimme, S. Density functional theory with London dispersion corrections. *WIREs Comput Mol Sci.* **2011**, *1*, 211–228.
53. Lu, T.; Chen, F. Multiwfn: a multifunctional wavefunction analyzer. *J. Comput. Chem.* **2012**, *33*, 580–592.
54. Zhang, J.; Lu, T. Efficient evaluation of electrostatic potential with computerized optimized code. *Phys. Chem. Chem. Phys.* **2021**, *23*, 20323–20328.
55. Wang, J.; Wolf, R.M.; Caldwell, J.W.; Kollman, P.A.; Case, D.A. Development and testing of a general amber force field. *J. Comput. Chem.* **2004**, *25*, 1157–1174.
56. Abraham, M.J.; Murtola, T.; Schulz, R.; Páll, S.; Smith, J.C.; Hess, B.; Lindahl, E. GROMACS: High performance molecular simulations through multi-level parallelism from laptops to supercomputers. *Softwarex* **2015**, *1-2*, 19–25.
57. Muntean, S.A.; Gerasimov, R.A.; Lyulin, A.V. Dynamics of water near oxidized polystyrene films. *Macromol. Theory Simul.* **2012**, *21*, 544–552.
58. Wu, C.; Chan, K.K.; Woo, K.F.; Qian, R.Y.; Li, X.H.; Chen, L.S.; Napper, D.H.; Tan, G.L.; Hill, A.J. Characterization of pauci-chain polystyrene microlatex particles prepared by chemical initiator. *Macromolecules* **1995**, *28*, 1592–1597.
59. Towler, P.; Staker, B.; Prasad, S.G.; Menon, S.; Tang, J.; Parsons, T.; Ryan, D.; Fisher, M.; Williams, D.; Dales, N.A.; Patane, M.A.; Pantoliano, M.W. ACE2 X-ray structures reveal a large hinge-bending motion important for inhibitor binding and catalysis. *J. Biol. Chem.* **2004**, *279*, 17996–18007.

Preprints (www.preprints.org) | NOT PEER-REVIEWED | Posted: 19 May 2023 doi:10.20944/preprints202305.1428.v1

60. Humphrey, W.; Dalke, A.; Schulten, K. VMD: visual molecular dynamics. J. Mol. Graph. **1996**, *14*, 33–38.
61. Guex, N.; Peitsch, M.C. SWISS-MODEL and the Swiss-PdbViewer: an environment for comparative protein modeling. *Electrophoresis* **1997**, *18*, 2714–2723.
62. Anandakrishnan, R.; Aguilar, B.; Onufriev, A.V. H++ 3.0: automating p*K* prediction and the preparation of biomolecular structures for atomistic molecular modeling and simulations. *Nucleic Acids Res.* **2012**, 40, 537–541.
63. Hornak, V.; Abel, R.; Okur, A.; Strockbine, B.; Roitberg, A.; Simmerling, C. Comparison of multiple Amber force fields and development of improved protein backbone parameters. *Proteins* **2006**, 65, 712–725.
64. Ma, Y.; Zydney, A.L.; Chew, J.W. Membrane fouling by lysozyme: Effect of local interaction. *AlChE J.* **2021**, *67*, e17212.
65. Essmann, U.; Perera, L.; Berkowitz, M.L.; Darden, T.; Lee, H.; Pedersen, L.G. A smooth particle mesh Ewald method. *J. Chem. Phys.* **1995**, *103*, 8577–8593.
66. Bussi, G.; Donadio, D.; Parrinello, M. Canonical sampling through velocity rescaling. *J. Chem. Phys.* **2007**, *126*, 14101.
67. Hess, B.; Bekker, H.; Berendsen, H.J.C.; Fraaije J.G.E.M. LINCS: A linear constraint solver for molecular simulations. *J. Comput. Chem.* **1997**, *18*, 1463–1472.
68. Berendsen, H.J.C., Postma, J.P.M., van Gunsteren, W.F., Hermans, J. Interaction models for water in relation to protein hydration. *Intermolecular forces*; Pullman, B., Eds.; Springer: Dordrecht, Netherlands, 1981; Volume 14, pp. 331–342.
69. Wang, X.; Wang, M.; Wei, Q.; Yang, X.; Yang, Y.; Cui, B.L.; Yang, X.N.; Xu, Z.J.; Modulation of solid-water-peptide interfacial properties towards surface adsorption/bioresistance. *Appl. Surf. Sci.* **2019**, *483*, 373–382.
70. Alsharif, S.A.; Power, D.; Rouse, I.; Lobaskin, V. In silico prediction of protein adsorption energy on titanium dioxide and gold nanoparticles. *Nanomaterials* **2020**, *10*, 1967.
71. Nakano, C.M.; Ma, H.; Wei, T. Study of lysozyme mobility and binding free energy during adsorption on a graphene surface. *Appl. Phys. Lett.* **2015**, *106*, 153701.